Dielectrophoretic Assembly of Nanowires

Yaling Liu, Jae-Hyun Chung,† Wing Kam Liu,* and Rodney S. Ruoff

Department of Mechanical Engineering, Northwestern University, 2145 Sheridan Road, Evanston, Illinois 60208-3111

Received: March 6, 2006; In Final Form: May 1, 2006

Nanowire (NW) assembly is currently of great interest, partly because NWs are considered as a fundamental component in the fabrication of a variety of devices. A powerful method has been developed to model the assembly of NWs. The three-dimensional dielectrophoretic (DEP) assembly of NWs across opposing electrodes is, for the first time, comprehensively studied using this new method. It is found that the DEP force reaches a maximum when the ratio of gap size to NW length is in the range 0.85−1.0. Both the magnitude and sign of the DEP torque on each NW varies with this ratio, and also with the orientation angle and the geometry and configuration of the electrode. The simulation of the dynamic assembly of individual and bundled NWs agrees with experiment. This method is of sufficient power that it will be of direct use in modeling DEP-based assembly and thus the manufacturing of nanoelectronic devices.

I. Introduction

Since the discovery of multiwalled carbon nanotubes in 1991,[1−6] various molecular electronic devices[1−5] have been proposed using nanotubes and nanowires. A stable electrical connection to the nanostructures is essential to achieve such nanoscale devices, and thus several methods[7−9] have been developed to assemble nanostructures onto electrodes. Among them, electric field guided assembly in a fluid offers the possibility of convenient and precise alignment of nanostructures across opposing electrodes.

Rod-shaped nanostructures have been assembled by electric field driven forces.[10,11] Individual multiwalled carbon nanotubes (MWCNTs) were assembled with high yield on an array of microelectrodes using the *composite electric-field guided assembly* approach.[8] These electric field-based methods offer room-temperature fabrication with rapid assembly of NWs, and if further developed, may be compatible with manufacturing of nanoelectronic devices.[12,13] However, the mechanisms underlying electric field-driven assembly have yet to be fully understood due to the complex nature of the three-dimensional electrohydrodynamic processes. In addition, the in-situ assembly process of NWs cannot be readily observed under a light microscope, which has hindered the study of the assembly mechanism, and hence, modeling electric field driven assembly faithfully becomes more important.

The dielectrophoretic (DEP) forces are widely used to manipulate micro and nanoscale particles.[14] The DEP force arises from an induced dipole moment embedded in a nonuniform electric field.[15] The force on the induced dipole can be written as $\mathbf{f}_{\mathrm{DEP}} = (\mathbf{p}\cdot\nabla)\mathbf{E}$, where $\mathbf{p}$ is the dipole moment and $\mathbf{E}$ is the electric field. A time-averaged DEP force on a particle can be approximated by replacing $\mathbf{p}$ with the effective dipole moment (EDM) of the particle.[15] This approach was used in the simulation of dielectrophoretic separation of carbon nanotubes.[16] However, the EDM approximation is valid only when the particle size is much smaller than the characteristic length of the electric field such that the electric field should not be disturbed by the presence of the particle. The EDM approximation is not valid for objects comparable in size to or larger than the gap between opposing electrodes or when the interaction of multiple particles has to be considered. To account for large particles, multipolar correction terms [15,17,18] may be added for accurate modeling, but such correction is still limited to spherical/prolate particles. Another method, called the image method,[15] analytically calculates the electric field near a surface using imaginary dipoles to obtain boundary conditions. The method is, however, only applicable to simple problems on multiple dipole interactions of one or two spherical particles. The problems on complex boundaries, such as multiple nonspherical particles surrounded with the semi-circular shaped electrodes discussed in this research, may not be solved by this method. To obtain a solution for the DEP force on high-aspect ratio NWs in the vicinity of microelectrodes under an electric field, it is essential to solve the electric field as a boundary value problem and numerically compute the DEP force using the Maxwell stress tensor (MST) method.[19] A detailed discussion on the applicability of EDM and MST theories is presented in Appendix A. In addition, the complex fluid dynamics during the assembly process cannot be understood by adding a simple friction term [16] to the equations of motion of the NW. Such a situation arises when NWs move close to the electrodes or assemble into bundles.

This paper presents, for the first time, simulation results for the three-dimensional dynamic electric field-guided assembly of NWs in a fluid using the immersed electrokinetic finite element (IEFEM) method [Figure 1], which is based on the immersed finite element method and electrokinetic theory. The immersed finite element method[20,21] is developed by merging the concept of immersed boundary,[22−24] finite element, and meshfree[25,26] methods for nonlinear fluids and solids. In IEFEM, independent solid meshes move on top of a fixed background fluid and electric field mesh during the simulation. This simple strategy removes the expensive mesh-updating cost and enables an efficient coupling of immersed NWs with the surrounding

* Corresponding author. Phone: +1−847-491-7094. Fax: +1−847-491-3915. E-mail: w-liu@northwestern.edu.

† Current address: University of Washington, Department of Mechanical Engineering, Campus Box: 352600, Seattle, WA 98195-2600.

10.1021/jp061367e CCC: $33.50
Published on Web 07/06/2006

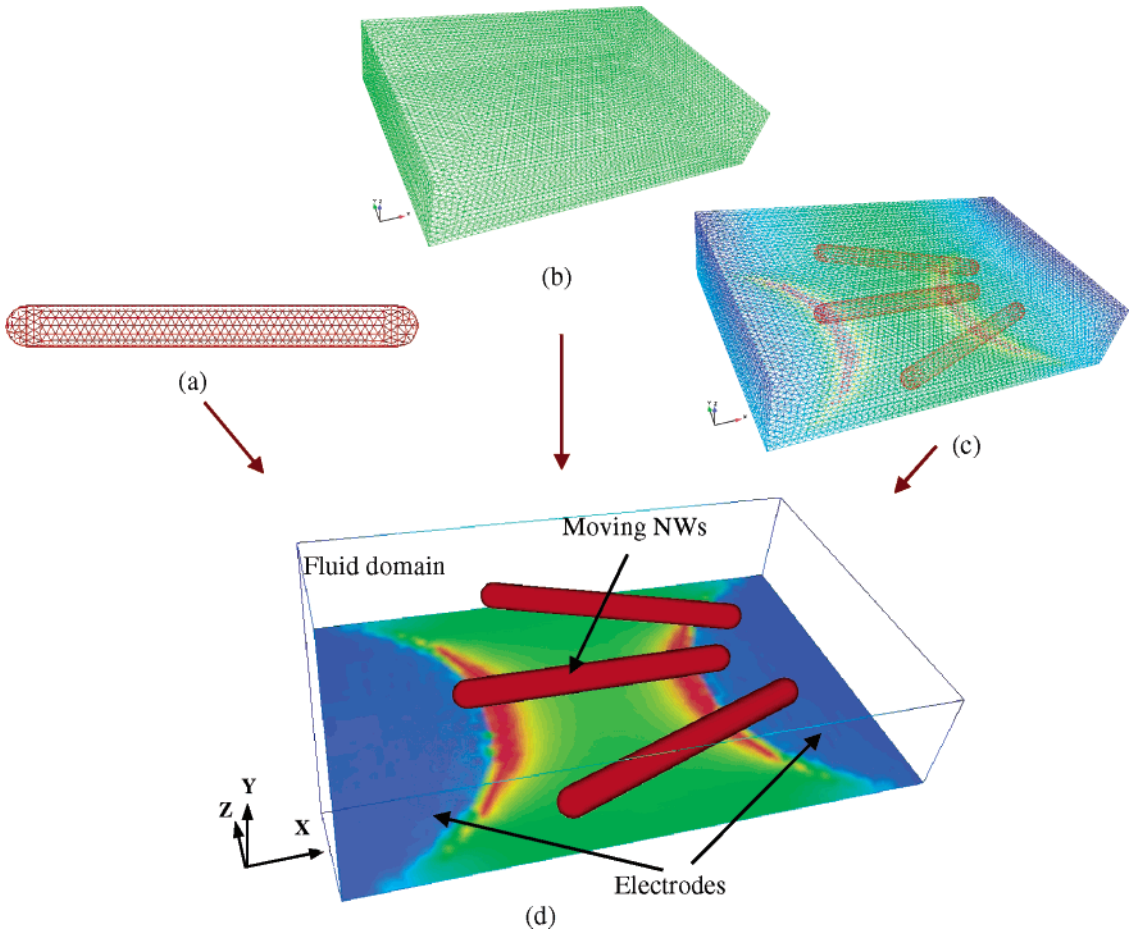

Figure 1. Conceptual illustration of the simulation method. (a) NWs are modeled as a moving rigid body with a Lagrangian mesh. (b) The Navier−Stokes equations are solved in the fluid domain with a fixed Eulerian mesh. (c) The electric field is solved in the whole domain with the domain occupied by the NWs traced individually (different electrical properties are assigned to the fluid domain and the NWs domain). (d) The motion of NWs, fluid dynamics and electric field are coupled together to simulate the NW assembly process. The color indicates the electric field strength on the substrate surface.

viscous fluid in the presence of an electric field. Dielectrophoretic forces and torques are analyzed to understand the patterns of assembled NWs. The assembly of both individual and multiple NWs on and near opposing electrodes are investigated through the analysis and compared with experimental results. A detailed description on the IEFEM is described in Appendix B.

The amplitude of the "nominal electric field" (defined as the applied voltage/smallest gap size between electrodes) used in our simulation is 0.5 V/μm. The frequency of the AC field is 5 MHz, under which no electro-osmotic flow is generated due to ion movement, according to analysis presented in Appendix C. The NW diameters are 200 nm, and their lengths are varied. In the simulation, they are initially assumed to be individually suspended in a solution. The viscosity of the solution at room temperature is $\mu = 0.78$Pa•s. The DC permittivities and conductivities of the solution and the NWs used in the simulation are $\epsilon^f = 20\epsilon_0$, $\sigma^f = 0.0056$ s/m and $\epsilon^s = 100\epsilon_0$, $\sigma^s = 0.0112$ s/m (ϵ_0: the permittivity of free space), respectively, in which the superscript f stands for fluid and s for solid. These values are chosen such that the complex permittivities of the solution and medium have an imaginary and real part in the same order of magnitude, i.e., 0.18−0.18i nF/m and 0.9−0.36i nF/m, respectively. Thus both real and imaginary parts contribute to the DEP force calculation. Based on the chosen AC frequency and electrical properties of the solution and NWs, the sign of the DEP force is positive and thus NWs will be attracted to the higher gradient of electric field. The contact resistances of NW-substrate and among contacting NWs are assumed to be infinite, i.e., the deposition and linking of NWs would not short-circuit the electric current.

NWs will be attracted by the DEP force toward a region where the gradient of the electric field is highest. When the length of a NW approaching the gap between opposing microelectrodes is comparable to the gap size, the electric field around the NW is distorted due to the existence of the NW [Figure 2a and b]. The time-averaged DEP force on a particle is calculated through a surface integral of the Maxwell stress $\mathbf{F}_{DEP} = \int_{\Gamma^s} (\sigma^M \cdot \mathbf{n}) dA$, where σ^M is the Maxwell stress (defined in Appendix eq s5), and $\mathbf{n}$ is the normal unit vector of the surface.

II. Dielectrophoretic Force and Torque

Since the assembly process is dynamic, the DEP force and torque vary at different stages of the process. As a parametric study, we chose a few specific configurations where the NWs are located at the center of the electrodes. In such configurations, all the NWs are dominated by dielectrophoretic force rather than other forces by Brownian motion, etc. Whether a NW can be trapped and properly aligned is determined by the strength of the DEP force and torque when it passes by the center of the gap. Although we have treated several specific configurations that seem most relevant for qualitative comparison with the experiment, we emphasize that the theoretical and computational framework is completely general and can be used for any

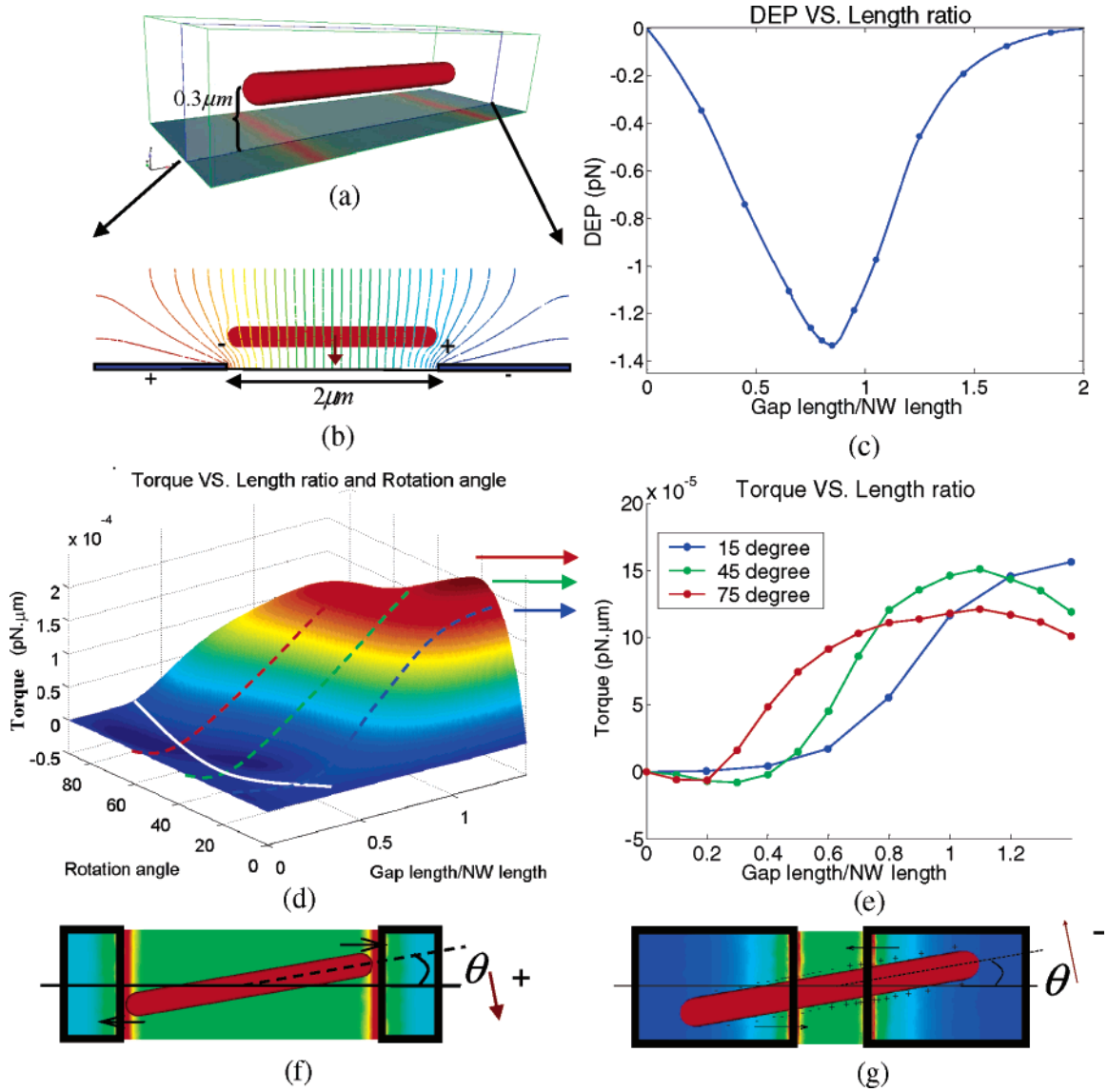

Figure 2. (a) A 2.0 μm long NW aligns across an opposing pair of coplanar rectangular-shaped electrodes at a height of 0.3 μm (b) Cross-sectional view: nonuniform electric field between two coplanar and opposing rectangular-shaped electrodes. The electric field near the NW is distorted due to its presence. (c) DEP force on a NW maintained at fixed height for various values of λ. (d) DEP torque on a NW between two parallel-rectangular shaped electrodes for various λ as a function of θ. (e) DEP torque for various λ at values of θ of 15, 45, 75 degrees. (f) An illustration of the $\lambda = 1$, $\theta = 10$ degree case, where the torque acts to rotate the NW back to the center line of the gap. (g) Illustration of the $\lambda = 0.25$, $\theta =$ 10 degree case, where the torque is negative and acts to rotate the NW away from the center-line.

configuration. It is found that the DEP force varies according to the ratio of the gap size to the NW length denoted by λ; to achieve a maximum DEP force, the gap size should be chosen by considering the length of a NW. In these simulations, the NW length l is 2.0 μm and the NW is constrained to lie in a plane 0.3 μm above the substrate [Figure 2a, b]. The NW is oriented perpendicular to the electrode edge with its center located at the midpoint of the gap. The ratio (λ_{f_max}) where the DEP force reaches a maximum is 0.85 [Figure 2c]; the combined effect of electric field strength and gradient is largest at this ratio. For $\lambda < \lambda_{f\_max}$, the DEP force is reduced by decreasing the gap size because, despite the imposed constant electric field strength (0.5 V/μm) at the midpoint of the gap, the electric field around the NW is weakened. For $\lambda > \lambda_{f\_max}$, the DEP force also decreases with increasing gap size because the electric field gradient around the NW is smaller. λ_{f_max} increases from 0.85 to 1 as the vertical position of the NW increases from 0.3 to 3.0 μm.

The DEP torque determines the orientation of the NWs. The DEP torque on a particle is calculated by $\gamma^{s}_{DEP} = \int_{\Gamma} \mathbf{r} \times (\sigma^{M} \cdot \mathbf{n}) dA$. The DEP torque is investigated by varying the ratio λ. A 2 μm-long NW is positioned at the same vertical position, 0.3 μm above the substrate as shown in Figure 2, but the initial angle of the NW (θ) varies from 0° to 90°. When the tilt angle is 0° or 90°, no DEP torque is exerted on the NW. The maximum DEP torque is observed at a tilt angle close to 30° [Figure 2d].

For parallel electrodes terminating in a rectangular shape, the torque could be positive such that the NWs are driven into alignment with the microelectrode pair, or could be negative such that the NWs are driven to be aligned orthogonal to the microelectrode pair. In the general case, the minimum energy configuration will be with the particle long axis aligned with the electric field. However, when the gap size is much smaller than the NW length ($\lambda < 0.3$), the short axis of the NW is found to be aligned with the electric field, leading to a negative torque

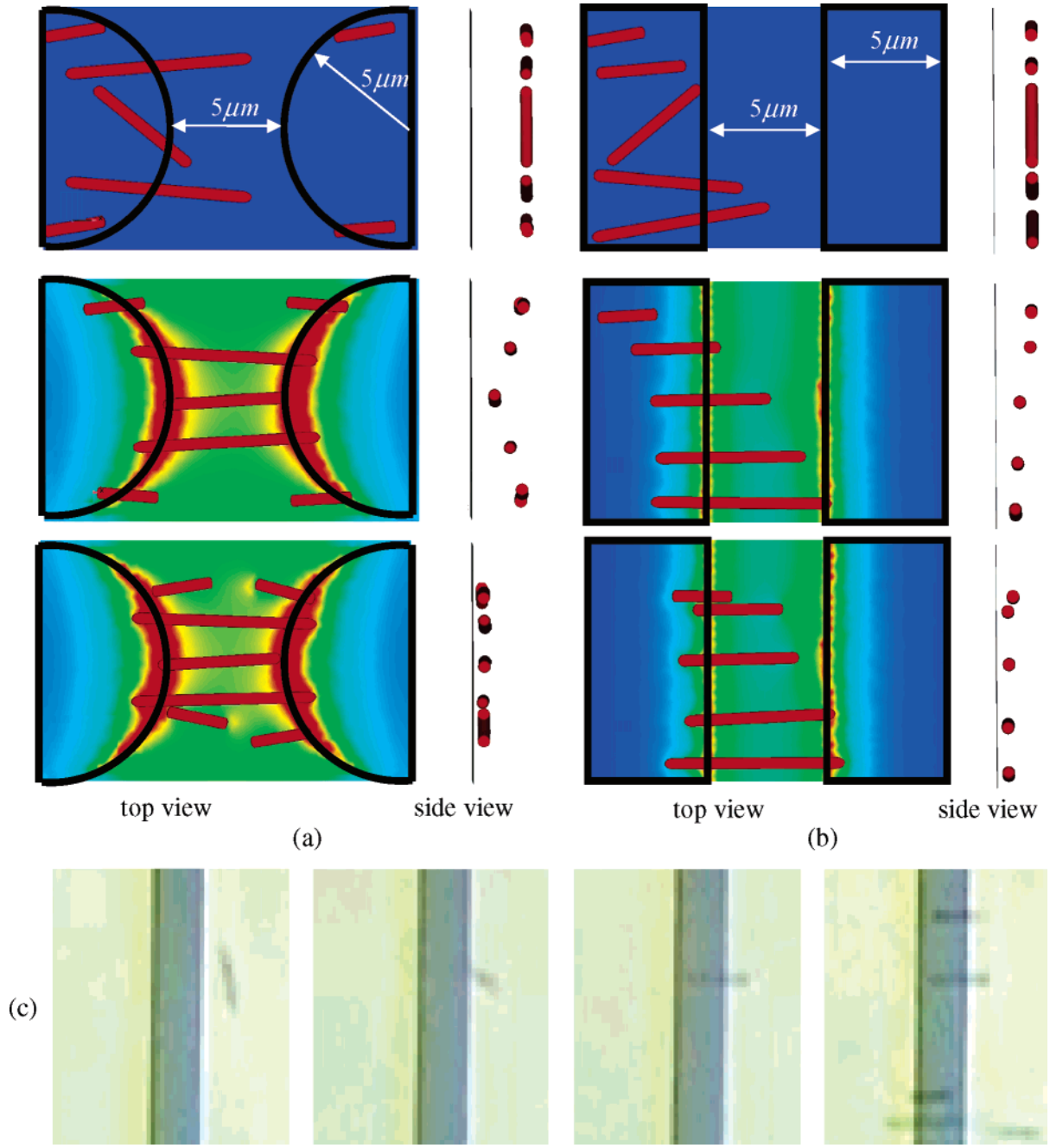

Figure 3. Simulation results of the assembly of NWs under an AC field (0.5V/μm at 5 MHz). Two pairs of semi-circular shaped and parallel-rectangular shaped electrodes are used with a gap size of 5 μm. The three sets of figures correspond to: (a) The assembly of 7 NWs between semi-circular shaped electrodes; (b) The assembly of 5 NWs between parallel-rectangular shaped electrodes; (c) Experimental images of SiC nanowires deposited on and near opposing electrodes; each figure shows sequential deposition in time of the SiC nanowires

[Figure 2e]. In such a case, the "effective axis" of the NW is not the long axis (length), but the short axis (diameter), thus the NW is aligned orthogonal to the electric field. The generation of such a negative torque is also illustrated by the nonuniform charge distribution on the NW surface [Figure 2g]. A critical ratio of $\lambda_{t\_critical}$ is found to lie between 0.2 and 0.4, where the sign of the torque changes. When λ is smaller than $\lambda_{t\_critical}$, the torque is close to zero or negative because both ends of the NW (itself longer than the gap size) are located far away from the electrode edge where the electric field is very small [Figure 2e]. Therefore, nanowires longer than the gap size by two or more times are likely to be mis-oriented with respect to the microelectrode pair. For $\lambda > \lambda_{t\_critical}$, the torque is always positive and the NWs are always driven into alignment with the microelectrode pair. The maximum torque is found for λ between 1.0 and 1.5 when the two ends of the NWs coincide with the highest electric field gradient regions [Figure 2f]. A similar trend is found for the DEP torque acting on a NW between two electrodes terminating in a semicircle, which is shown in Figure S1 in the Supporting Information.

III. Assembly of Individual Nanowires

A pair of semi-circular shaped electrodes ($R = 5.0$ μm, minimum gap length 5 μm) and a pair of rectangular-shaped electrodes are used to investigate the assembly of an array of NWs using DEP. Five to seven NWs are randomly positioned initially in the computational domain [Figure 3a and b]. The influence of NW length on assembly is investigated by varying the lengths of the NWs (with a mean of 5 μm). For long NWs

(small λ), the NWs are not well oriented along the electric field between the two electrodes. When the ratio is close to 1.0, the NWs are well aligned. For the shorter NWs ($\lambda = 2.0$), the NWs are deposited at the edges of the electrodes. The simulation pattern agrees with the experimental image shown in Figure 3c. The experimental details are described in the Appendix D. It is found that the velocity of each NW when approaching the electrodes is size dependent. When all NWs are initially placed in a plane 2 μm above the electrodes, the longer NW deposit first and the shorter NWs deposit last because of the larger DEP force on the longer NWs. This time dependence suggests a possibility of sorting NWs according to their lengths by designing electrodes with different gap sizes. For example, when NWs of various lengths are transported with a constant velocity across an array of electrodes with different gap sizes, it is apparent that most of the NWs deposited on these electrodes should have a length close to the corresponding gap size. In the simulation of the assembly of seven NWs between semicircular shaped electrodes, it is found that longer NWs are deposited across the electrodes in a parallel pattern, while shorter NWs are deposited close to the edge of the electrodes in a direction perpendicular to the electrodes (Figure 3a).

Sequential experimental images of the assembly of NWs are shown in Figure 3c. SiC NWs with lengths close to 10 μm are oriented "properly" on the 10 μm-wide gaps, whereas NWs much longer than 10 μm are not properly oriented or positioned outside the gaps. This observation is consistent with our simulation results. The modeling results also show that NWs much longer than the gap size are attracted to span the 10 μm-wide gaps only when they are very close to the bottom of the substrate initially; this is because the DEP force dramatically increases as the height decreases. Another observation from these simulations is that when two NWs deposit close to each other, a third longer NW may be deposited across them with its two ends connecting the ends of the deposited NWs (Supporting Information, Figure S2(a)). This deposition pattern is due to the fact that a high electric field region is created at the ends of each of the initially deposited NWs, and the two ends of the third longer NW are "trapped" by these high electric field regions during deposition. This pattern is also observed in the experiment (Supporting Information, Figure S2(b)).

IV. Bridge/fibril Formation of Nanowires

Bundle formation is essential to achieve function for certain types of nanoelectronic devices.[27] When the gap size in the simulation is much larger than the NW length (e.g., $\lambda = 6.0$), NW fibrils formed between electrodes. The NW fibril is created by the following sequence of events (Figure 4): (1) NWs present around a gap are oriented along the direction of the electric field. (2) NWs close to the tip of the electrodes are attracted toward the tip (where the electric field gradient is the highest). (3) Subsequently, a high-strength and high-gradient electric field is generated at both ends of the assembled NWs because of the high aspect ratio of the NWs. (4) The NWs form local bundles due to the interaction between neighboring NWs. (5) Such local bundles link together, transported toward the center, and finally bridge the gap. This dynamic process is somewhat difficult to observe in real time in experiments due to the small size of NWs, but is clearly demonstrated in the simulation. Similar bundle assembly patterns have been observed with spherical particles[28,29] called pearl-chain formation. The patterns obtained in our simulation are also observed for DEP assembly of SWCNTs between two electrodes terminating in a triangle or semicircle, see Figure 10 in ref 30 and Figure 2 in ref 31.

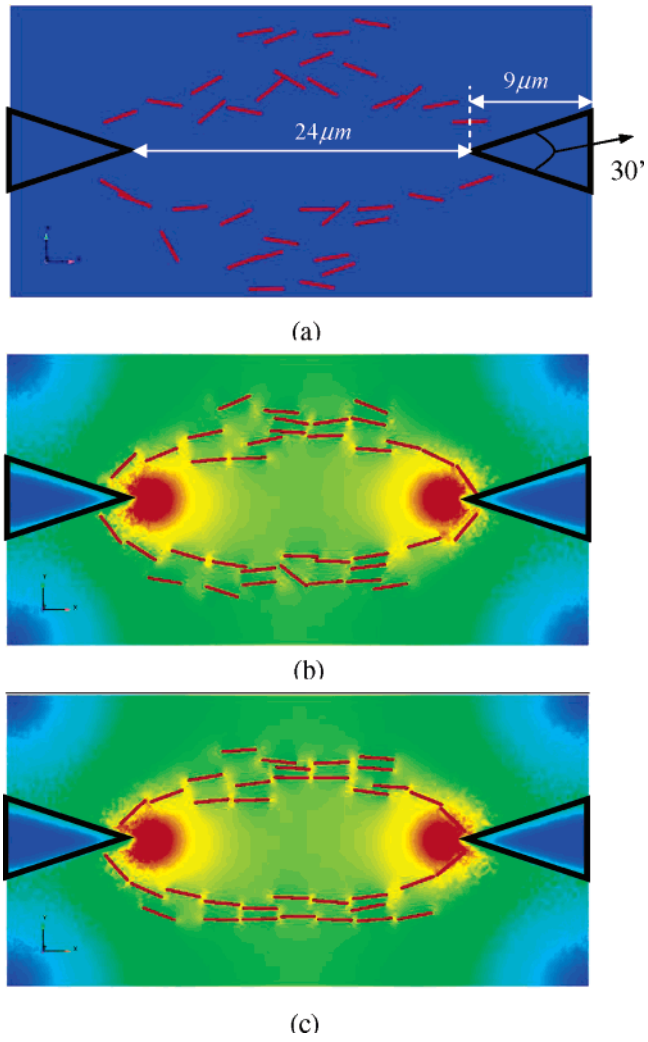

Figure 4. Sequential images of 3 μm-long NWs lining up between triangular-shaped electrodes (angle: 30°). AC field of 5 MHz (0.5V/μm) is applied between electrodes (gap size: 24 μm). (a) $t = 0$ s; (b) $t = 0.5$ s; (c) $t = 1.0$ s.

V. Conclusions

In summary, electric field driven assembly of NWs in a liquid between and near opposing microelectrodes is studied for the first time with a three-dimensional electro-hydrodynamic simulation method. The dielectrophoretic force and torque acting on an individual NW depend on the geometries of both the microelectrodes and the NWs. The force and torque are analyzed to develop an understanding of the pattern of deposited NWs for a given set of geometries and initial conditions. The assembly of individual NWs between opposing electrodes is demonstrated and compared with experimental results for deposited NWs. Understanding of the process of NW fibril formation is developed through these simulations. The IEFEM method presented here is a powerful modeling and simulation tool for developing fundamental understanding of electrokinetic phenomena. To our knowledge, there does not exist another simulation method that can produce the results (Figures 2 and 3) presented in this paper. While our focus here has been on the dielectrophoretic force acting on large-aspect-ratio nanowires (which is both inadequately and inappropriately treated by the standard electric dipole method), it is likely that the IEFEM method will find use in modeling many other electrokinetic phenomena, including those present in biological systems. We

suggest that it will also shorten the cycle for manufacturing assembled nanostructures for a variety of useful applications.

Acknowledgment. We appreciate discussion of SiC NW geometry and physical properties with X. Chen and I. Jung. The support of this research by the Office of Naval Research (ONR) and the National Science Foundation (NSF) is gratefully acknowledged. We also acknowledge partial support from DTRA.

Supporting Information Available: Five figures and a link to movies showing additional details of the assembly of individual nanowires. This material is available free of charge via the Internet at http://pubs.acs.org.

Appendix

A. Effective Dipole Moment theory and Maxwell Stress Tensor theory. The EDM theory assumes that only a single dipole is induced on a particle. The particle is assumed to be small compared to the characteristic length of the external electric field, so that the gradient of the electric field (∇E) is essentially constant in the region surrounding the particle. In addition, it is assumed that the existence of the particle does not disturb its surrounding electric field. Based on these assumptions, a widely used expression for the time-averaged DEP force on a particle is given by the EDM theory as the following:

$$\langle \mathbf{F}_{\mathrm{DEP}} \rangle = \Gamma \epsilon_1 \mathrm{Re}\{K_{\mathrm{f}}\} \nabla(E^2) \qquad \text{(s1)}$$

where Γ is a geometric parameter that depends on the particle shape and size; ϵ_1 is the real part of the permittivity of the medium; K_f is the polarization factor that depends on the complex permittivities of both the particle and the medium; E is the root-mean-square magnitude of the local electric field. For a spherical particle with radius a, $\Gamma = 2\pi a^3$, and $K_f = (\tilde{\epsilon}_2 - \tilde{\epsilon}_1)/(\tilde{\epsilon}_2 + 2\tilde{\epsilon}_1)$ (the Clausius−Mossotti factor). The frequency-dependent complex permittivities are expressed by the complex combination of conductivity (σ), permittivity (ϵ), and the angular velocity of the electric field (ω) as $\tilde{\epsilon}_1 = \epsilon_1 - j\sigma_1/\omega$, and $\tilde{\epsilon}_2 = \epsilon_2 - j\sigma_2/\omega$, where $j = \sqrt{-1}$, and the indices 1 and 2 refer to the medium and the particle, respectively.

As mentioned before, eq s1 is valid only when the dimension of a particle is much smaller than the characteristic length scale of the electric field. The EDM theory is not applicable to the NW assembly because NWs are positioned in the vicinity of electrodes. In addition, only a few analytical solutions for DEP forces on particles with simple geometries are available, such as a sphere, or a prolate/oblate particle. Hence, the EDM theory is not applicable to particles with other complex geometries, such as the hexagonal cross section SiC NWs discussed here. The MST theory is required for the calculation of DEP force on the particles close to the electrodes.

As a further test of the MST method used in the simulation, a spherical particle with a diameter of 2 μm is placed at the 10 μm-high position above a 8 μm-wide gap between two parallel electrodes with an applied voltage of 4 V. The center of the particle is placed at the midpoint of the gap. Both the MST and the EDM theories give a DEP force $\sim 2.2 \times 10^{-13}$N. A comparison in closer proximity to the electrodes (e.g., 0.5 μm-high position) or for a comparably larger particle (e.g., with a diameter of 10 μm) is not possible, because of the large variation of ∇E; the MST model can yield correct forces acting on the sphere, but the EDM model cannot. A detailed comparison for EDM and MST used to calculate DEP force in single electrode traps has been performed by Rosales and Lim.[32] They showed that multipolar terms should be considered to obtain accurate results for spheres in the proximity of the electrodes, and full MST calculation is required in the study of nonspherical particles. It should be noted that the DEP force in the vicinity of the electrodes is crucial in determining the final assembly pattern of, e.g., high aspect ratio nanostructures such as NWs.

TABLE 1: Summary of Electrodynamics Nomenclature

name	symbol
voltage or potential difference	V
electric field potential	ϕ
electric field intensity	E
permittivity	ϵ
conductivity	σ
complex permittivity	$\tilde{\epsilon} = \epsilon + (\sigma/j\omega)$

B. Simulation Method and Simulation Details. The proposed IEFEM method is developed based on the immersed finite element method (IFEM)[20,33] which improves computational efficiency by avoiding mesh-regeneration. In IEFEM, a moving NW coexists with a fixed mesh of Eulerian fluid and the electric field (Supporting Information Figure S3). The electric field is solved using general continuum electro-mechanics, and the DEP forces on the NWs are numerically evaluated through the MST theory. Fluid, electric field, and NW domains are coupled together through finite element formulation and the interface between the fluid and NW subdomains are enforced via a mapping function.[25,26] Through the simulation method, the dynamic process of the attraction, alignment, and deposition of the NWs between microelectrodes is modeled by solving for DEP, electrokinetics, fluid flow, and NW motions. The details of the method are described at length in the following. Consider a domain Ω enclosed with a sufficiently smooth boundary $\Gamma^f = \partial\Omega$ as shown in Figure S3. Suppose there exists a submerged solid domain Ω^s enclosed by a boundary Γ^s, the entire domain Ω is subdivided into two regions, namely, the solid region Ω^s and the fluid region $\Omega\backslash\Omega^s$. Therefore, the interface between the solid and fluid regions can be simply expressed as $\Gamma^s = \partial\Omega^s$. The Eulerian description is used for the fluid domain while the Lagrangian description is employed for the solid domain. The electric field is calculated in the entire domain Ω. We assume that the material properties are constant (i.e., electric conductivity and permittivity) in the fluid and the NWs, and the time scale of the motion of the NWs is much larger than the electric field and no body net charge exist.

For currents and frequencies typically found in DEP assembly problems, the governing equations of the electric field can be described by the reduced quasi-electrostatic form of the Maxwell equations:[14]

$$\nabla\cdot(\epsilon\mathbf{E}) = \rho_f \qquad \text{Gauss equation}$$

$$\mathbf{E} = -\nabla\phi \qquad \text{the electric field is irrotational}$$

$$\frac{\partial\rho_f}{\partial t} + \nabla\cdot(\sigma\mathbf{E}) = 0 \qquad \text{the charge conservation equation}$$

Where ρ_f is the free charge density, $\mathbf{E}$ is the electric field intensity, ϵ is the permittivity of the material, and σ is the conductivity of the material.

Under an AC field with an angular frequency ω and $\partial\rho_f/\partial t = j\omega\rho_f$, we use complex values such that $\tilde{\epsilon} = \epsilon + (\sigma/j\omega)$, the

coupled free charge/current Maxwell equation can be reduced into a simpler form in complex variables:

$$\nabla\cdot(\tilde{\epsilon}^f\nabla\tilde{\phi}^f) = 0, \text{ in } \Omega\backslash\Omega^s \tag{s2}$$

$$\nabla\cdot(\tilde{\epsilon}^s\nabla\tilde{\phi}^s) = 0, \text{ in } \Omega^s \tag{s3}$$

where $\tilde{\phi}$ is the complex electric field potential, $\tilde{\epsilon}$ is the complex permittivity, with $\tilde{\epsilon} = \epsilon + (\sigma/j\omega)$, and the superscripts s and f refer to the solid (particle) and fluid, respectively.

The normal component of the total current at the solid and fluid interface has to be continuous:

$$\tilde{\epsilon}^s\tilde{\mathbf{E}}^s\cdot\mathbf{n} = \tilde{\epsilon}^f\tilde{\mathbf{E}}^f\cdot\mathbf{n}, \text{ on } \Gamma^s \tag{s4}$$

The interface is updated along with the solid domain through the Lagrangian description: $\Gamma^s = \partial\Omega^s$.

The Maxwell stress tensor is defined as $\tilde{\mathbf{T}}^M = \mathrm{Re}(\tilde{\epsilon})(\tilde{\mathbf{E}}\tilde{\mathbf{E}} - 1/2\tilde{\mathbf{E}}\cdot\tilde{\mathbf{E}}\mathbf{I})$, where $\mathbf{I}$ is an identity tensor. If we write the electric field intensity into a sum of a complex variable $\tilde{\mathbf{E}}$ and its complex conjugate $\tilde{\mathbf{E}}^*$ as $\mathbf{E} = 1/2(\tilde{\mathbf{E}} + \tilde{\mathbf{E}}^*)$, the time-averaged net DEP force on a particle can be calculated through a surface integral of the Maxwell stress[19] as $\mathbf{F}_{\mathrm{DEP}} = \int_{\Gamma^s}(\sigma^M\cdot\mathbf{n})\mathrm{d}A$, where

$$\sigma^M = \frac{1}{4}\mathrm{Re}(\tilde{\epsilon})((\tilde{\mathbf{E}}\tilde{\mathbf{E}}^* + \tilde{\mathbf{E}}^*\tilde{\mathbf{E}}) - |\tilde{\mathbf{E}}|^2\mathbf{I}) \tag{s5}$$

B1. Immersed Finite Element Method Coupled with Electrokinetics. In this manuscript, we consider an incompressible viscous fluid described by the Navier−Stokes equations:

$$\nabla\cdot\mathbf{v} = 0, \text{ in } \Omega\backslash\Omega^s \tag{s6}$$

$$\rho\dot{\mathbf{v}} = \nabla\cdot\sigma, \text{ in } \Omega\backslash\Omega^s \tag{s7}$$

where $\mathbf{v}$ is the fluid velocity, ρ is the fluid density, and σ is the fluid Cauchy stress tensor. Gravitational force and Brownian motion are not considered here due to negligible influence on the motion of particles close to electrodes.[34,35] An order of magnitude analysis of AC electroosmosis flow, Brownian motion, and temperature gradient is given in Appendix C.

For an incompressible Newtonian fluid of uniform viscosity, σ can be written as

$$\sigma = -p\mathbf{I} + \mu(\nabla\mathbf{v} + (\nabla\mathbf{v})^T) \tag{s8}$$

where μ is the fluid viscosity and p is the fluid pressure.

The governing equation for a general deformable solid is described as

$$\rho^s\dot{\mathbf{v}}^s = \nabla\cdot\sigma^s + \nabla\cdot\sigma^M, \text{ in } \Omega^s \tag{s9}$$

where $\mathbf{v}^s$ is the solid velocity, ρ^s is the solid density, σ^s is the solid stress tensor, and σ^M is the Maxwell stress defined in eq s5. For a rigid particle (i.e., a NW), we have $\sigma^s = 0$. Moreover, rigid constraints are applied onto the solid domain to get the average velocity with the conservation of total linear and angular momentum:

$$\mathbf{V}_i^s = \frac{1}{m_i^s}\int_{\Omega_i^s}\rho^s\mathbf{v}^s\mathrm{d}\Omega \tag{s10}$$

$$\omega_i^s = \frac{1}{I_i^s}\int_{\Omega_i^s}\rho^s\mathbf{r}^s\times(\mathbf{v}^s - \mathbf{V}_i^s)\mathrm{d}\Omega \tag{s11}$$

where $\mathbf{r}^s = \mathbf{x} - \mathbf{x}_{\mathrm{center},i}$, m_i^s and I_i^s are the mass and moment of inertia of the ith particle, and $\mathbf{V}_i^s$ and ω_i^s are the linear and angular velocities of the ith particle.

The velocity of the solid domain occupied by the ith particle is thus rewritten in terms of linear and angular velocities

$$\mathbf{v}^s = \mathbf{V}_i^s + \omega_i^s\times\mathbf{r}^s \tag{s12}$$

To avoid the computationally expensive re-meshing usually encountered in the fluid-structure interaction problems, an extra force is introduced onto the whole domain Ω, so that the domain occupied by the solid will behave like a solid (described by eq s9), while the domain not occupied by the solid will behave as a pure fluid (described by eq s7). This extra force, called the fluid-structure interaction force, is added to the R.H.S of eq s7, thus extending the calculation domain from $\Omega\backslash\Omega^s$ to Ω.

Rewriting the solid eq s9 with $\sigma^s = 0$ into the form of eq s7 and by noting that $\mathbf{v}^s = \mathbf{v}$ in Ω^s, we have the following:

$$\rho^s\dot{\mathbf{v}}^s = \nabla\cdot\sigma^M + (\rho^s - \rho)\dot{\mathbf{v}}^s + \nabla\cdot\sigma - \nabla\cdot\sigma^M + \mathbf{F}^{\mathrm{FSI}}, \text{ in } \Omega^s \tag{s13}$$

$\mathbf{F}^{\mathrm{FSI}}$ is the interacting force exerted on the fluid by the solid and it has compact support on Ω^s. On the fluid domain $\Omega\backslash\Omega^s$, we know, obviously, that $\mathbf{F}^{\mathrm{FSI}}$ must vanish. Thus, the interacting force $\mathbf{F}^{\mathrm{FSI}}$ can be defined as the following:

$$\mathbf{F}^{\mathrm{FSI}} = \begin{cases} -(\rho^s - \rho)\dot{\mathbf{v}}^s + \nabla\cdot(-\sigma + \sigma^M), & \text{in } \Omega^s \\ 0, & \text{in } \Omega\backslash\Omega^s \end{cases} \tag{s14}$$

Based on eq s14, eq s7 can be extended to the whole domain as

$$\rho\dot{\mathbf{v}} = \nabla\cdot\sigma + \mathbf{F}^{\mathrm{FSI}}, \text{ in } \Omega \tag{s15}$$

Moreover, a restriction operator L_t^s from Ω onto Ω^s is needed to make the system complete, An Eulerian to Lagrangian mapping is defined as

$$(L_t^s\psi)(\mathbf{X},t) \equiv \psi(\mathbf{x}(\mathbf{X},t),t), \forall\ \mathbf{X}\in\Omega_0^s \tag{s16}$$

With this mapping function, we obtain the solid velocity from the Eulerian space as

$$\mathbf{v}^s = L_t^s\mathbf{v}, \text{ in } \Omega^s \tag{s17}$$

It plays a role in identifying the solid velocity field from the fluid velocity on Ω^s. For the sake of simplicity, we chose a Dirac Delta function as the restriction mapping for solid velocity (the reproducing kernel particle method[25,26] (RKPM) delta function employed in IEFEM can handle both uniform and nonuniform grids that enables us to deal with fluid domains with arbitrary geometries).

In a similar way, we can obtain the immersed formulation for electric field potential by extending eq s2 into the whole domain Ω:

$$\nabla\cdot(\tilde{\epsilon}^f\nabla\tilde{\phi}) + Q = 0 \tag{s18}$$

where

$$\tilde{\phi} = \begin{cases} \tilde{\phi}^s, & \text{on } \Omega^s \\ \phi^f, & \text{on } \Omega\backslash\Omega^s \end{cases} \tag{s19}$$

$$Q = \begin{cases} \nabla\cdot((\tilde{\epsilon}^s - \tilde{\epsilon}^f)\nabla\tilde{\phi}^s), & \text{in } \Omega^s \\ 0, & \text{in } \Omega\backslash\Omega^s \end{cases} \quad \text{(s20)}$$

Here, Q represents the influence of the induced dipoles of the solid on the electric field. A mapping function based on FEM-basis functions is used to obtain the electric field potential in the solid domain from the Eulerian space:

$$\tilde{\phi}^s = L_t^s\tilde{\phi}, \text{ in } \Omega^s \quad \text{(s21)}$$

In summary, the governing equations involved in the electrokinetic coupling are as follows:

$$\nabla\cdot(\tilde{\epsilon}^f\nabla\tilde{\phi}) + Q = 0, \text{ in } \Omega \quad \text{(s22)}$$

$$Q = \begin{cases} 0, & \text{in } \Omega\backslash\Omega^s \\ \nabla\cdot((\tilde{\epsilon}^s - \tilde{\epsilon}^f)\nabla\tilde{\phi}), & \text{in } \Omega^s \end{cases} \quad \text{(s23)}$$

$$\tilde{\phi}^s = L_t^s\tilde{\phi} \text{ in } \Omega^s \quad \text{(s24)}$$

$$\rho^f\left(\frac{\partial\mathbf{v}}{\partial t} + \mathbf{v}\cdot\nabla\mathbf{v}\right) = \nabla\cdot\sigma + \mathbf{F}^{\mathrm{FSI}}, \text{ in } \Omega \quad \text{(s25)}$$

$$\mathbf{F}^{\mathrm{FSI}} = \begin{cases} (\rho - \rho^s)\dot{\mathbf{v}}^s + \nabla\cdot(-\sigma + \sigma^{\mathrm{M}}), & \text{in } \Omega^s \\ 0, & \text{in } \Omega\backslash\Omega^s \end{cases} \quad \text{(s26)}$$

$$\mathbf{v}^s = L_t^s\mathbf{v} \text{ in } \Omega^s \quad \text{(s27)}$$

Boundary conditions:

$$\mathbf{v} = 0, \text{ at substrate surface} \quad \text{(s28)}$$

$$\mathbf{n}\cdot(\tilde{\epsilon}^s\tilde{\mathbf{E}}^s - \tilde{\epsilon}^f\tilde{\mathbf{E}}^f) = 0, \text{ at solid-fluid interface } \Gamma^s \quad \text{(s29)}$$

$$\tilde{\phi} = \tilde{\phi}_0, \text{ at electrode surfaces} \quad \text{(s30)}$$

These equations are put into their weak forms and solved numerically using the finite element method. In this way, the equations of nanowire motion, fluid flow, and electric field are combined together. In the simulation presented here, the equation for the electric field and fluid/NW motion equation are solved iteratively.

The simulations are carried out by the immersed electrokinetic finite element code, which is written in Fortran 90 and developed at Northwestern University. The visualizations are performed by the commercial software ENSIGHT (CEI Inc.). Three-dimensional tetrahedral elements are used in the simulations. The fluid mesh has 42 677 nodes and 22 6532 elements. Each nanowire is discretized into 1536 nodes and 6253 elements. A time step of 0.001 s is chosen in our simulation and each step takes around one minute in a PC with 2.0GHz CPU.

C. Order of Magnitude Analysis of Various Factors. Factors other than electrical and viscous forces may also influence the particle motion. An order of magnitude analysis of AC electroosmosis flow, Brownian motion, and temperature effect is presented below.

C1. AC Electroosmosis Flow. The AC electroosmosis flow is driven by the electrostatic force applied to the charged double layer on the surfaces of the electrodes. The sign of the ions in the double layers is always opposite to the charges on the corresponding electrode surfaces. To generate a cumulative effect, i.e., steady flow, the sign alternation speed of the AC field should be slower than the response time of the ions.

The response time of the ions in a liquid is characterized by the charge relaxation time, which is the ratio of liquid permittivity to conductivity:

$$\tau = \epsilon/\sigma \quad \text{(s31)}$$

If the AC frequency $f < 1/(2\pi\tau)$, the motion of ions in the double layer leads to a steady flow. In the case of ethanol, the time constant $\tau = 1.7$ ms. An AC frequency of 5 MHz is used in the experiments (i.e., $f \gg 1/(2\pi\tau)$), and thus no AC electro-osmosis flow will be generated at such a frequency.

C2. Brownian Motion. Diffusion due to Brownian motion leads to random motion of submicron particles. However, recent experimental work showed that the DEP force required to induce the motion of submicrometer particles is in the scale of sub-pico Newton.[36] A scaling analysis is conducted to explain that the Brownian motion does not significantly influence DEP trapping.

The random displacement of a particle due to Brownian motion follows a Gaussian profile in one dimension with a mean squared displacement given by[37]

$$|\Delta x|^2 = 2Dt \quad \text{(s32)}$$

where the diffusion coefficient $D = k_BT/\gamma$, and γ is the drag coefficient.

The displacement due to Brownian motion in a time period t is

$$|\Delta x| = \sqrt{\frac{2k_BT}{\gamma}t} \quad \text{(s33)}$$

The terminal velocity of a particle under a constant DEP force f_E can be expressed as $u = f_E/\gamma$, thus the displacement due to DEP force in time period t is

$$\Delta x = u\cdot t = f_E/\gamma t \quad \text{(s34)}$$

The ratio of displacement induced by Brownian motion and the displacement induced by DEP force is given as

$$\alpha_{\text{Brownian/DEP}} = \frac{\sqrt{\frac{2k_BT}{\gamma}t}}{\frac{f_E}{\gamma}t} = \frac{\sqrt{2k_BT\gamma/t}}{f_E} \quad \text{(s35)}$$

Let's assume that a sphere with radius $a = 1$ μm is assembled at room temperature at the height of 5.0 μm. For a spherical particle, $\gamma = 6\pi\mu a$. The DEP force f_E is usually on the order of *pN* and is chosen to be 5 pN here. For a time period of one second, $\alpha_{\text{Brownian/DEP}}$ is around 0.05. Thus, the effect of Brownian motion can be neglected in our simulation.

C3. Thermal Effect. The electric field can induce temperature increase of the fluid due to Joule-heating. The temperature increase can be described as follows:[35]

$$\Delta T = \frac{\sigma V^2}{2k} \quad \text{(s36)}$$

where σ and k are the electrical and thermal conductivity of the fluid, respectively, and V is the voltage applied on the electrode.

For ethanol, $\sigma = 0.13$ μS/m[38] and $k = 0.169$ W/m·K.[38] Under the applied voltage of 4 V in the experiment, $\Delta T = 6.2 \times 10^{-6}$ K, so the effect of temperature increase is negligible.

D. Experimental. To observe the assembly process of SiC NWs (length range: 10−100 μm, diameter range: 300−500 nm; Advanced Composite Materials Corporation, Greer, SC; "ACMC"), 10 μm-wide gaps are prepared on a 500 nm-thick oxide-on-Silicon wafer substrate (Figure 3c). The NWs are suspended in an ethanol solution and an AC field ($10V_{pp}$, 5 MHz) is applied. The SiC NWs are dominated by a positive DEP at an AC field of 5 MHz considering the electric properties of ethanol and SiC NWs (the DC permittivities of ethanol and SiC NWs are $\epsilon^f = 24.6\epsilon_0$[39] and $\epsilon^s = 9.72\ \epsilon_0$,[40] respectively. The conductivities of ethanol and SiC NW at room temperature are $\sigma^f = 0.13\ \mu$S/m[38] and $\sigma^s = 6.16$ S/m, respectively). The conductivity of SiC NWs used in this experiment is obtained by two probe measurement (Supporting Information, Figure S4). The electrical connection at both ends of the SiC NWs is achieved by two consecutive runs of Ti/Au films (150/50 nm); these consecutive depositions of Ti/Au films lead to the formation of continuous metal contacts on the 500 nm-diameter SiC NWs. Note that the permittivity of some colloidal suspensions is frequency dependent,[41] and thus the assumption of constant permittivity may break down at certain frequencies. This issue will be addressed in our future work.

In addition, the cross-section of most of the SiC NWs in the experiment is hexagonal (SEM images by Dr. Xinqi Chen are shown in Supporting Information Figure S5). In the modeling, the DEP force of the hexagonal cross-section is about 10% smaller than that of the circular cross-section, which has only a minor effect on the final assembly pattern of the NWs.

Note Added after ASAP Publication. This article was published ASAP on July 3, 2006. The journal cited in ref 19 was changed. The revised article was reposted on July 6, 2006.

References and Notes

(1) Chen, R. J.; Bangsaruntip, S.; Drouvalakis, K. A.; Kam, N. W. S.; Shim, M.; Li, Y. M.; Kim, W.; Utz, P. J.; Dai, H. J. *Proc. Natl. Acad. Sci. U.S.A.* **2003**, *100*, 4984.

(2) Cui, Y.; Wei, Q. Q.; Park, H. K.; Lieber, C. M. *Science* **2001**, *293*, 1289.

(3) Huang, Y.; Duan, X. F.; Wei, Q. Q.; Lieber, C. M. *Science* **2001**, *291*, 630.

(4) Li, C.; Zhang, D. H.; Liu, X. L.; Han, S.; Tang, T.; Han, J.; Zhou, C. W. *Appl. Phys. Lett.* **2003**, *82*, 1613.

(5) Ng, HT, H. J., Yamada, T, Nguyen, P.; Chen, Y. P.; Meyyappan, M. *Nano Lett.* **2004**, *4*, 1247.

(6) Iijima, S. *Nature* **1991**, *354*, 56.

(7) Rao, S. G.; Huang, L.; Setyawan, W.; Hong, S. H. *Nature* **2003**, *425*, 36.

(8) Chung, J. Y.; Lee, K. H.; Lee, J. H.; Ruoff, R. S. *Langmuir* **2004**, *20*, 3011.

(9) Cassell, A. M.; Franklin, N. R.; Tombler, T. W.; Chan, E. M.; Han, J.; Dai, H. J. *J. Am. Chem. Soc.* **1999**, *121*, 7975.

(10) Smith, P. A.; Nordquist, C. D.; Jackson, T. N.; Mayer, T. S.; Martin, B. R.; Mbindyo, J.; Mallouk, T. E. *Appl. Phys. Lett.* **2000**, *77*, 1399.

(11) Chen, X. Q.; Saito, T.; Yamada, H.; Matsushige, K. *Appl. Phys. Lett.* **2001**, *78*, 3714.

(12) Qian, D.; Wagner, G. J.; Ruoff, R. S.; Yu, M. F.; Liu, W. K. *Appl. Mech. Rev.* **2002**, *55*, 495.

(13) Lee, Y. C.; Parviz, B. A.; Chiou, J. A.; Chen, S. *IEEE Trans. on Adv. Packag.* **2003**, *26*, 217.

(14) Green, N. G.; Morgan, H. *AC Electrokinetics—Colloids and Nanoparticles*; Research Studies Press: 2003.

(15) Jones, T. B. *Electromechanics of particles*; Cambridge University Press: New York, 1995.

(16) Dimaki, M.; Boggild, P. *Nanotechnology* **2004**, *15*, 1095.

(17) Jones, T. B. *IEEE Eng. Med. Biol. Magn.* **2003**, *22*, 33.

(18) Schnelle, T.; Muller, T.; Fiedler, S.; Fuhr, G. *J. Electrost.* **1999**, *46*, 13.

(19) Wang, X.; Wang, X. B.; Cascoyne, P. R. C. *J. Electrost.* **1997**, *39*, 277.

(20) Zhang, L.; Gerstenberger, A.; Wang, X. D.; Liu, W. K. *Comput Method Appl. M* **2004**, *193*, 2051.

(21) Liu, W. K.; Liu, Y.; Farrell, D.; Zhang, L.; Wang, X.; Fukui, Y.; Patanker, N.; Zhang, Y.; Bajaj, C.; Lee, J.; Hong, J.; Chen, X.; Hsu, H. Immersed Finite Element Method and Applications to Biological Systems. *Comput. Methods Appl. Mech. Eng.* **2006**, *195*, 1722−1749.

(22) Peskin, C. S. *Acta Numerica* **2002**, *11*, 479.

(23) Peskin, C. S.; Mcqueen, D. M. *J Comput Phys* **1980**, *37*, 113.

(24) McQueen, D. M.; Peskin, C. S. *J. Supercomput.* **1997**, *11*, 213.

(25) Li, S. F.; Liu, W. K. *Meshfree Particle Methods*; Springer, 2004.

(26) Liu, W. K.; Jun, S.; Zhang, Y. F. *Int. J. Numer. Methods Fluids* **1995**, *20*, 1081.

(27) Tang, J.; Gao, B.; Geng, H. Z.; Velev, O. D.; Qin, L. C.; Zhou, O. *Adv Mater* **2003**, *15*, 1352.

(28) Docoslis, A.; Alexandridis, P. *Electrophoresis* **2002**, *23*, 2174.

(29) Kretschmer, R.; Fritzsche, W. *Langmuir* **2004**, *20*, 11797.

(30) Chung, J.; Lee, J. *Sens. Actuators, A* **2003**, *104*, 229.

(31) Zhang, J.; Tang, J.; Yang, G.; Qiu, Q.; Qin, L. C.; Zhou, O. *Adv. Mater.* **2004**, *16*, 1219.

(32) Rosales, C.; Lim, K. M. *Electrophoresis* **2005**, *26*, 2057.

(33) Wang, X. D.; Liu, W. K. *Comput Method Appl M* **2004**, *193*, 1305.

(34) Pohl, H. A. *Dielectrophoresis*; Cambridge University Press: Cambridge, 1978.

(35) Ramos, A.; Morgan, H.; Green, N. G.; Castellanos, A. *J. Phys. D Appl. Phys.* **1998**, *31*, 2338.

(36) Morgan, H.; Green, N. G. *J. Electrost.* **1997**, *42*, 279.

(37) Einstein, A. *Investigations on the Theory of Brownian Movement*; New York: Dover: 1956.

(38) Dean, J. A. *Lange's Handbook of Chemistry*, 14th ed.; McGraw-Hill: 1992.

(39) http://www.clippercontrols.com/info/dielectric_constants.html.

(40) Patrick, L.; Choyke, W. J. *Physical Review B* **1970**, *2*, 2255.

(41) Jimenez, M. L.; Arroyo, F. J.; Turnhout, J.; Delgado, A. V. *J. Colloid Interface Sci.* **2002**, *249*, 327.